IVYSPRING
INTERNATIONAL PUBLISHER

Theranostics

2017; 7(13): 3276-3292. doi: 10.7150/thno.19987

Research Paper

Biodegradable Hollow Mesoporous Silica Nanoparticles for Regulating Tumor Microenvironment and Enhancing Antitumor Efficiency

Miao Kong[1, 2], Jiamin Tang[3], Qi Qiao[1], Tingting Wu[1], Yan Qi[1], Songwei Tan[1, 4], Xueqin Gao[1], Zhiping Zhang[1, 4, 5]✉

1. Tongji School of Pharmacy, Huazhong University of Science and Technology, Wuhan 430030, China;
2. Department of Pharmacy, Sanmenxia Central Hospital, Sanmenxia 472000, China;
3. China Three Gorges University, Yichang 443002, China;
4. National Engineering Research Center for Nanomedicine;
5. Hubei Engineering Research Center for Novel Drug Delivery System, Huazhong University of Science and Technology, Wuhan 430030, China.

✉ Corresponding author: Prof. Dr. Zhiping Zhang, Wuhan 430000, P. R. China Fax and Phone: +86-27-83601832 E-mail: zhipingzhang@mail.hust.edu.cn

Received: 2017.03.08; Accepted: 2017.05.29; Published: 2017.07.23

Abstract

There is accumulating evidence that regulating tumor microenvironment plays a vital role in improving antitumor efficiency. Herein, to remodel tumor immune microenvironment and elicit synergistic antitumor effects, lipid-coated biodegradable hollow mesoporous silica nanoparticle (dHMLB) was constructed with co-encapsulation of all-trans retinoic acid (ATRA), doxorubicin (DOX) and interleukin-2 (IL-2) for chemo-immunotherapy. The nanoparticle-mediated combinational therapy provided a benign regulation on tumor microenvironment through activation of tumor infiltrating T lymphocytes and natural killer cells, promotion of cytokines secretion of IFN-γ and IL-12, and down-regulation of immunosuppressive myeloid-derived suppressor cells, cytokine IL-10 and TGF-β. ATRA/DOX/IL-2 co-loaded dHMLB demonstrated significant tumor growth and metastasis inhibition, and also exhibited favorable biodegradability and safety. This nanoplatform has great potential in developing a feasible strategy to remodel tumor immune microenvironment and achieve enhanced antitumor effect.

Key words: nanoparticles, tumor microenvironment, immunosuppression, drug delivery, cancer treatment.

Introduction

Cancer treatment still remains great challenge despite the fact that some current therapies like surgery, chemotherapy, radiotherapy and immunotherapy can combat tumor and control tumor progression during initial treatment [1]. This may be attributed to the complicated tumor microenvironment, which consists of tumor cells, immune cells, stromal cells, extracellular matrix and so on [2]. Immune system plays a vital role in modulating tumor progression and thus how to induce potent antitumor immunity is a key in the success of immunotherapy [3]. However, insufficiency of immune effector cells infiltration [4] and existence of immunosuppressive cells/compounds in tumor microenvironment [3] seriously block the efficiency of immune system. Simply relying on immunotherapy against tumor microenvironment is far from enough. Therefore, new therapeutic strategies, like the combination of chemotherapy and immunotherapy (chemo-immuno-therapy), emerge to achieve synergistic effect by tumor microenvironment regulation [5]. In this combination, chemotherapeutic agents not only exert direct lethal effect on tumor cells, but also have demonstrated the capability of inducing immunogenic cells death (ICD) [6, 7] or directly decreasing suppression on immune effector cells [8-11] in low dosage. Accordingly, immunotherapy can increase the sensibility of cancer cells to chemotherapeutic agents and reduce undesired side effects [12].

Tumor-induced immunosuppression is one of the important obstacles affecting immune system function in tumor microenvironment [13]. The accumulation of immunosuppressive cells, such as myeloid-derived suppressor cells (MDSCs), contributes to tumor evasion of immune surveillance [14]. In pathological situation, differentiation of myeloid cells will be partially blocked, resulting in accumulation of immature myeloid cells which are called MDSCs and can upregulate the immunosuppressive factors to suppress T cell functions [13, 15]. Considering that MDSCs contribute to negative regulation of antitumor immune responses, depleting MDSCs becomes a key to reverse immunosuppression in tumor microenvironment. Only in the case of immunosuppression relieved, immune agents will be able to play their role in activating innate and adaptive immune functions, which can develop synergistic effect with chemotherapeutic agents in the combinational therapy.

Based on above presumption of chemo-immunotherapy, we introduced a kind of biodegradable hollow mesoporous silica nanoparticle (dHMSN) for co-delivery of doxorubicin (DOX), all-trans retinoic acid (ATRA) and interleukin-2 (IL-2) to achieve enhanced antitumor efficiency in chemo-immunotherapy. DOX, a wide-spectrum antineoplastic agent, induces serious side effects at high dosage [16], while low dosage of DOX treatment is more favorable in inducing antitumor immunity with less toxicity. ICD effect induced by DOX can increase immunogenicity of tumor which makes remained cancer cells more susceptible to the recognition of cytotoxic T lymphocytes (CTLs) [17, 18]. ATRA has been officially approved in the treatment of acute promylocytic leukemia [19, 20]. For cancer treatment, ATRA can induce the differentiation of cancer stem cells mediated by retinoic acid and retinoid X receptors, thus sensitizing tumor cells to chemotherapy [21-23]. Besides, it is reported that ATRA can differentiate MDSCs into mature dendritic cells (DCs), macrophages, and granulocytes and improve tumor-specific immune response [24, 25]. So ATRA holds great potential for regulating MDSC-induced immunosuppression. IL-2, as a T cell growth factor, can facilitate the proliferation and activation of tumor-infiltrating T lymphocytes and natural killer (NK) cells [26]. IL-2 has been approved by FDA for advanced metastatic melanoma treatment [27]. However, co-delivery of these agents with distinctly different physicochemical properties is a great challenge for conventional nanocarriers. Fortunately, HMSN has been developed for multifunctional drug co-delivery due to its favorable core-shell structure, large surface area, tunable pore size and shell thickness. It has provided excellent drug loading capacity not only for small molecules, but also for proteins, nucleic acids, fluorescent dyes, etc. [28-33]. Considering that the issue of retention and metabolism about nanosilica in human body is still concerned [34-36], the biodegradability and biocompatibility of HMSN should be taken into consideration to realize a safer and more reliable nanocarrier for cancer treatment. In this study, we designed dHMSN which could degrade naturally in physiological condition. With co-encapsulation of ATRA and DOX along with the absorption of IL-2 on the surface through electronic interaction, dHMSN was further coated with a lipid bilayer (namely dHMLB) to improve the stability and biocompatibility. Eventually, we obtained a kind of biodegradable and safe nanocarrier to realize simultaneous delivery of three agents and achieve synergistic antitumor effect. The characteristics of nanoparticles, drug release profiles and biodistribution were evaluated. The therapeutic efficiency and involved immune responses were further investigated in murine melanoma models. This biodegradable nanoplatform may provide a promising strategy of tumor microenvironment modulation to realize synergistic antitumor efficacy in chemo-immunotherapy.

Materials and Methods

Synthesis of biodegradable HMSN

dHMSN was synthesized as described in Scheme 1. Solid SiO_2 core ($sSiO_2$) was firstly synthesized by a modified Stöber method [37]. 0.8 mL of ammonia solution and 5 mL of water were added to 35.7 mL of ethanol and stirred at 30°C for 30 min. Then, 1 mL of TEOS was added. The product was collected by centrifugation, washed several times and resuspended in water. Secondly, $sSiO_2$ coated with mesoporous SiO_2 shell ($mSiO_2$) was prepared by using CTAC as mesopore template. $sSiO_2$ suspension was added to the admixture of 6 g of CTAC, 0.18 g of TEA and 40 mL of water, followed by adding 20 mL of TEOS in cyclohexane (10 v/v %) with gently stirring. Thirdly, selective etching strategy was performed to obtain hollow core structure. The above mixture was dispersed in 120 mL of 0.2 M Na_2CO_3 solution with stirring at 50°C for 1 h and then centrifuged and washed. CTAC in mesopore was removed by ultrasonic extraction for three times using HCl/ethanol solution (v/v=1/10). After that, dHMSN with hollow core and biodegradable mesoporous shell was obtained.

Preparation of dHMLB

Thin-film hydration method was applied to prepare liposome, of which the composition mass ratio of DOPC, cholesterol and DSPE-PEG2000 was 10:3:0.5. Then liposome solution was serially extruded through 1.0, 0.4, 0.2 and 0.1 μm polycarbonate membrane and incubated with a certain amount of dHMSN for 2 h at 37°C with gentle shaking to form dHMLB.

Characterizations of dHMSN and dHMLB

Transmission electron microscope (TEM) images were taken on Tecnai G2 F30 (FEI Corporation, Dutch) for observing morphology and size distribution of dHMSN and dHMLB. The hydrodynamic diameter and zeta potential of dHMSN and dHMLB were measured by dynamic light scattering (DLS, Zeta Plus, Brookhaven Instruments, USA). *In vitro* stability of dHMLB in FBS was determined by DLS for 72 h, which was repeated in triplication. Fourier transform-infrared spectroscopy (FT-IR) by VERTEX 70 (Bruker Corporation, Germany), Brunauer-Emmett-Teller (BET) by TriStar II 3020 (Micromeritics, USA) and thermogravimetric analysis (TGA) by Pyris1 TGA (PerkinElmer Instruments, USA) were employed to characterize the nanoparticles.

In vitro biodegradation profile

Five milligram of dHMSN was dispersed in 50 mL of PBS (0.1 mg/mL) at 37°C for constant shaking. 4 mL of sample solution was taken out at assigned time intervals (12 h, 1 d, 2 d, 3 d, 5 d, 7 d) for centrifugation at 12000 rpm for 10 min. The supernatant was then extracted to determine the concentration of free silicon using inductively coupled plasma-mass spectrometry (ICP-MS, ELAN DRC-e, PerkinElmer, USA). TEM images were also taken at different intervals for qualitative degradation analysis of dHMSN.

In vitro cytotoxicity

Cytotoxicity of nanoparticles was determined by methyl thiazolyl tetrazolium (MTT) assay on L929 fibrosarcoma cells. Briefly, cells were seeded in 96-well plates (1×10^4 cells/well) and then treated with various concentrations of dHMSN or dHMLB. After incubation for 24 h, cell viability was determined by microplate reader (BioTek Synergy HT, USA). All the groups were performed in six parallel wells.

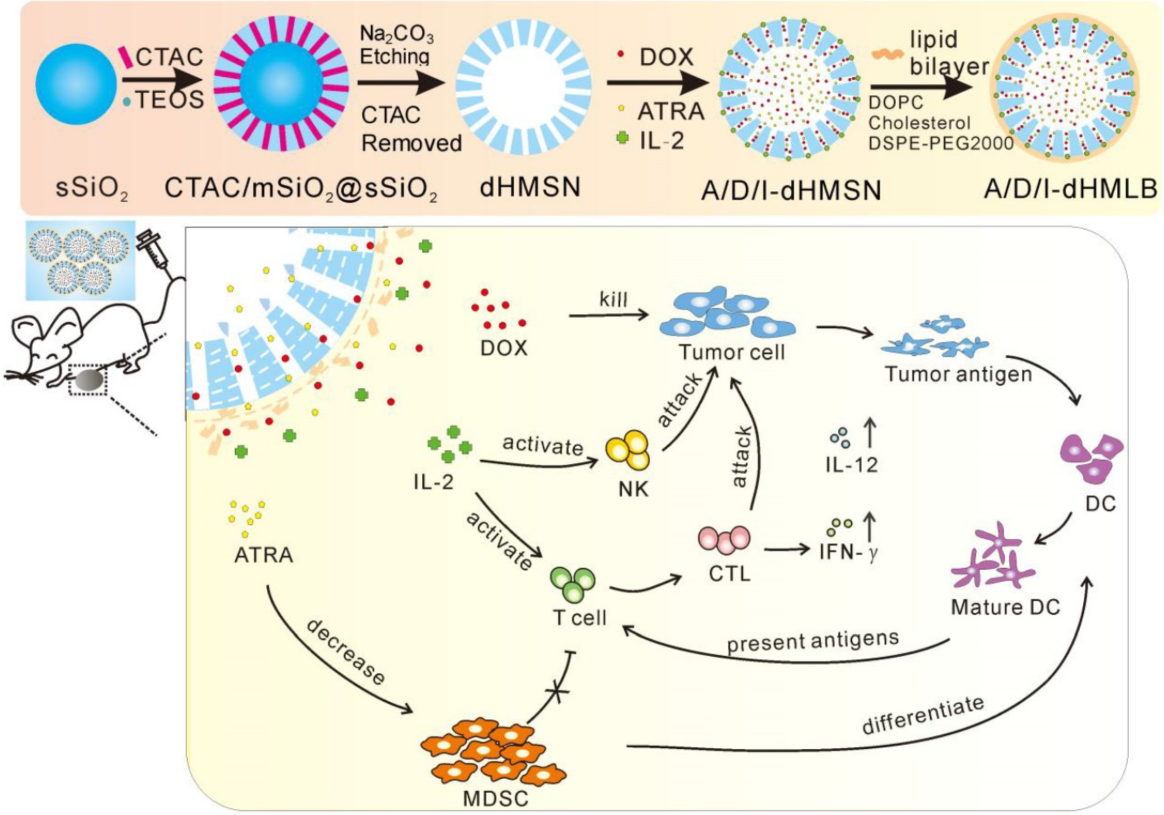

Scheme 1. The preparation of drug-loaded biodegradable lipid-coated hollow mesoporous silica nanoparticles (A/D/I-dHMLB) and schematic illustration of the induced synergistic antitumor efficiency of chemo-immunotherapy against cancer.

Hemolysis assay

Fresh blood was collected using heparinized tubes and washed twice with ice-cold PBS. The obtained red blood cells (RBCs) were diluted to 2% (w/v) by ice-cold PBS containing various concentrations (10, 25, 50, 100, 250, 500, 1000 and 5000 μg/mL) of dHMSN, dHMLB and polyethylenimine (PEI) (25 kDa), respectively, and then incubated for 4 h at 37°C. The samples were then centrifuged at 3000 rpm for 10 min, and the supernatant from each sample was determined on the absorbance at 540 nm by microplate reader. RBCs treated with distilled water and 1 x PBS were considered as the positive and negative control, respectively. The degree of hemolysis was determined by the following formula.

$$\mathrm{Hem}(\%) = (A_{\mathrm{Sample}} - A_0)/(A_{100} - A_0)\times 100\%$$

where A_{100} and A_0 were the absorbance of solution at 100% and 0% hemolysis, respectively.

Drug loading of dHMSN

Before drug loading, (3-aminopropyl) triethoxysilane (APTES) was used to modify dHMSN with amino ester to improve the loading efficiency (details shown in supporting information). Then, dHMSN was redispersed in ATRA solution (10 mg/mL in DMSO) and incubated for 12 h at 37°C. After removing free ATRA by centrifugation, ATRA-loaded dHMSN (A-dHMSN) was redispersed in DOX solution (10 mg/mL in water). After 4 h incubation, IL-2 was added and incubated for 12 h at 4°C. ATRA, DOX and IL-2 co-loaded dHMSN (A/D/I-dHMSN) was thus obtained after centrifugation and washing. A/D/I-dHMSN was then coated with lipid bilayer (A/D/I-dHMLB) using the similar method of preparing empty dHMLB. ATRA in supernatant was collected to quantify the drug loading efficiency (DLE) by high performance liquid chromatography (HPLC, Hitachi L-2000, Japan) equipped with a UV detector and a reverse phase TC-C18 column (150 mm × 4.6 mm, pore size 5 μm, Agilent, USA). The mobile phase is methanol/water/acetic acid (90:10:0.5, v/v). The flow rate is 1.0 mL/min and the detection wavelength is 360 nm. DOX in supernatant was quantified by microplate reader with excitation/emission wavelength at 485/590 nm. IL-2 in supernatant was detected by enzyme-linked immunosorbent assay (ELISA) kit according to the protocol (Dakewe biotech, China). The formula of calculating DLE was presented below.

$$\mathrm{DLE}\ (\%) = \frac{\text{weight of fed drug} - \text{weight of drug in supernatant}}{\text{weight of fed drug}} \times 100\%$$

In vitro drug release

In vitro drug release behaviors of A/D/I-dHMLB were performed *via* centrifugation method in PBS containing 0.2% Tween 80 with pH 7.4 and 6.8. Briefly, A/D/I-dHMLB was dispersed in 10 mL of release medium and put in shaking bath at a speed of 100 rpm at 37°C. At assigned interval of 0.5, 1, 2, 4, 8, 12, 24 h, the released sample was centrifuged and supernatant was collected for subsequent analysis. The same volume of fresh medium was immediately supplemented into the tube for continuous release. The supernatant was then extracted by chloroform to detect ATRA or DOX by HPLC and IL-2 in supernatant could be directly detected by ELISA. The extracted ATRA was detected by HPLC as above described. Analysis of DOX was performed by HPLC using a reverse phase Restek C18 column (150 mm × 4.6 mm, pore size 5 μm). The mobile phase is acetonitrile and 0.067 mM KH_2PO4 buffer (25:75, v/v, pH 4.21 adjusted with H_3PO_4) with a flow rate of 1.0 mL/min. The fluorescence detector was operated at 470/585 nm (excitation/emission).

Biodistribution and pharmacokinetic study

To determine the biodistribution of dHMLB in tumor-bearing mice, near-infrared fluorescent dyes Cy5-amine was loaded in dHMLB and intravenously (*i.v.*) injected to B16F10 tumor-bearing C57/BL6 mice. *In vivo* imaging of mice and *ex vivo* imaging of tumor were presented at different intervals post injection using an *in vivo* imaging system (IVIS) Lumina XR equipped with a 150 W quartz halogen lamp and 1 mW power scanning laser (Caliper Life Sciences, Hopkinton, USA). Acquired images were analyzed by Living Imaging software.

The content of elemental Si was also analyzed to further assess the biodistribution of dHMLB. Tumor-bearing mice were *i.v.* injected with 0.75 mg/mL dHMLB and sacrificed at 0 h, 6 h, 24 h and 48 h to analyze Si content in different organs (heart, liver, spleen, lung and kidney) and tumor *via* ICP-MS. 5 mL of 60% HNO_3 (ultrapure) was added to 30 mg lyophilized tissue and heated at 140°C for 4 h in perfluoroalkoxy alkane tubes. Then samples were diluted with Milli-Q water to 10 mL and measured by ICP-MS. Ge was used as the internal standard and Si was measured as ^{28}Si.

Pharmacokinetic study was conducted in healthy Sprague-Dawley (SD) rats (n=3) after *i.v.* injection of free ATRA, DOX, IL-2 and A/D/I-dHMLB at the dose of 15 mg ATRA/kg, 5 mg DOX/kg and 2.5 μg IL-2/kg, respectively. At pre-determined time of 0.5, 1, 2, 4, 8, 12 and 24 h, blood samples were collected using heparinized tubes. The samples were pretreated by centrifugation at 3000 rpm for 10 min and precipitation with methanol. Then ATRA or DOX was extracted with 1 mL chloroform by vortex for 5 min and detected by HPLC. IL-2 could be directly detected from plasma by ELISA. The pharmacokinetic parameters were calculated using drug and statistics software (version 2.1.1, Mathematical Pharmacology Professional Committee, China).

Antitumor activity in B16F10 tumor model

Tumor inhibition activity was evaluated in B16F10 tumor-bearing mice. Dosage of IL-2 was selected as 2.5 µg/kg according to the reported paper [38]. The ratio of ATRA/DOX was selected as 3/1 [23] and the dosage of DOX was primarily chosen as 0.5, 1, 2.5, 5.0 mg/kg. 5×10^4 B16F10 cells were subcutaneously injected into the right flank of C57BL/6 mice. After 7 days of transplantation, mice with tumor of 3-5 mm diameter were divided randomly into different groups. On day 7, 10, and 13 after tumor cells implantation, saline, A/D-dHMLB and A/D/I-dHMLB were *i.v.* administered, respectively. The tumor size and body weight of mice were measured every other day. Mice were sacrificed on day 18 and tumors were harvested for image and weight. The second exploration experiment was conducted to further confirm the optimized dosage and the followed formal inhibition experiment was conducted based on the exploration results. Tumor inhibitory rate was calculated and organ sections were treated with hematoxylin and eosin (H&E) staining.

Metastasis inhibition in B16F10 metastatic tumor model

The metastasis model was established by *i.v.* injection of 5×10^5 B16F10 cells to C57BL/6 mice on day 0. Mice were randomly divided into nine groups on day 1 followed by four times administration of saline, free drugs and drugs-loaded dHMLB, respectively (every three days). After twenty days, mice were sacrificed and lungs, kidneys, and livers were excised and photographed. Lungs were fixed in Bovin fixative solution and sections of organs were treated with H&E staining. The number of metastatic lung nodules was counted and metastatic inhibitory rate was calculated. S100 expression of lung was investigated through immunohistochemical staining.

Evaluation of systematic toxicity

Toxicity evaluation was conducted in tumor-bearing mice after three times administration. Serum chemistry levels including alanine aminotransferase (ALT), aspartate aminotransferase (AST) and blood urea nitrogen (BUN) from collected blood in every group were measured according to manufacturer's instruction (Nanjing Jiancheng Bioengineering Institute, China). All samples were repeated in triplication. Organs (heart, liver, spleen and kidney) were fixed in paraformaldehyde fixative solution for H&E staining.

Flow cytometric analysis of immune response

In order to investigate the immune response in tumor microenvironment, tumors were excised on the day after last administration to collect infiltrating immune cells. Briefly, tumor was weighed and digested with collagenase A and DNAse I in serum-free RPMI media for 80 min at 37°C. After filtered through 100 µm cell strainer (BD Biosciences, USA) and centrifuged at 2000 rpm for 5 min, cells were collected and then purified by mouse lymphocyte isolating solution. The isolated cell suspension was counted and pre-incubated with Fc blocking antibody (anti-CD16/CD32) for 10 min at 4°C to avoid non-specific binding. After that, cell suspension was divided for series of antibody staining to mark MDSC ($CD11b^+Gr\text{-}1^+$), DC ($CD11c^+$), mature DC ($CD11c^+CD86^+$), $CD8^+$ T cell ($CD3^+CD8^+$), activated $CD8^+$ T cell ($CD3^+CD8^+CD69^+$), $CD3^+CD8^+IFN\text{-}\gamma^+$ cell and NK cell ($CD3^-NK1.1^+$).

Cytokine analysis and immunofluorescence assay

Equal weight of tumors in every group was excised to investigate cytokines secretion (IL-12p70, IL-10, TNF-α, TGF-β and IFN-γ) in tumor microenvironment. After high speed homogenization and centrifugation, the supernatant was detected by ELISA. The collected blood samples were also analyzed to detect IFN-γ concentration in plasma. All of the samples were repeated in triplication. Tumor sections after treatment were taken to assay $CD3^+CD8^+IFN\text{-}\gamma^+$ T cells with immunofluorescence staining and representative immunofluorescence images were presented.

Statistical analysis

Statistical analysis was performed using a two-tailed Student's t test by comparing between two groups. Data are shown as means ± s.d.. Significant difference was presented as $^*p<0.05$, $^{**}p<0.01$, $^{***}p<0.001$.

Results and Discussion

Synthesis and characterization of dHMSN and dHMLB

dHMSN was synthesized in three steps of preparing solid core ($sSiO_2$), mesoporous shell ($CTAC/mSiO_2@sSiO_2$) and hollow core (dHMSN) as described in Scheme 1. We obtained a series of uniform dHMSN (~180 nm) with varied core size and shell thickness in Figure 1a. The diameter of hollow core depended on the size of $sSiO_2$. When adjusting the ratio of reagents in the first step, it could make different sizes of $sSiO_2$, thus obtaining different hollow core structure [37]. In the next step, CTAC was applied as the template to grow a mesoporous shell. The thickness and pore size could be adjusted by changing reaction time, organic solvent and TEOS concentration, and this novel biphase reaction endowed the shell with biodegradable feature [39]. In the final step, how to selectively etch solid silica core and protect the integrity of silica shell was the most important part of synthesis. As reported [40], the positive charge part of cationic surfactants, such as CTA^+ in CTAC, would absorb to the surface of silica shell *via* electronic attraction, thus leaving the shell intact in etching process. Indeed, silica shell was found to be destroyed in the case of washing off CTAC before etching process (as seen in supporting information Figure S1). Besides, we also explored the effect of Na_2CO_3 concentration and etching duration which should be strictly controlled in etching process (Figure S2). The optimal etching condition was finally determined as 0.2M Na_2CO_3 etching for 1 h at 50°C without washing off CTAC. After etching process, HCl/ethanol solution along with ultrasonic extraction was used to remove CTAC in mesopore. CTAC could be thoroughly removed as proved by FT-IR spectra in Figure 1b, where the peak of -CH- of CTAC disappeared after three times extraction. Nitrogen adsorption-desorption isotherms in Figure 1c showed a more evident hysteresis loop in dHMSN compared with $mSiO_2@sSiO_2$, which meant the elevated capillary condensation effect from the hollow core structure. dHMSN exhibited increased BET surface area of 939.2 m^2/g and pore volume of 30.03 mm^3/g as comparison with $mSiO_2@sSiO_2$ of 662.4 m^2/g and 17.28 mm^3/g, respectively. In Figure 1d, dHMSN revealed the bimodal pores and larger area under the curve, which also indicated the existence of hollow core structure and larger pore volume in nanoparticles. The hollow structure and increased surface area could greatly facilitate drug loading capability of dHMSN. Moreover, the biodegradation feature of dHMSN was evidenced from TEM images (Figure 1e), showing that the gradual degradation could be achieved in several days in simulated physical condition. *In vitro* biodegradation profile was also quantified by testing the degraded Si content in PBS (Figure 1f). dHMSN was degraded over 50% in three days and nearly 100% in seven days. The degraded profile and TEM images both confirmed the biodegradation property of dHMSN. It has been reported that the biodegradation capability of inorganic silica nanoparticles will be affected by many factors, such as the condensation of Si-O-Si network, surface area and pore size [41]. The prepared $mSiO_2$ by the heterogeneous reaction possessed low cross-linking degree of Si-O-Si framework, high surface area, large pores and thin pore wall [39], which may facilitate the rate of ionic corrosion from degradation media and thus contribute to the biodegradation property of dHMSN.

Considering the stability and biocompatibility of nanocarriers, we chose a kind of lipid bilayer composed of DOPC, cholesterol and DSPE-PEG2000 to coat dHMSN, *i.e.* dHMLB. TEM images (Figure 2a) demonstrated the structural integrity of the lipid coating, which was about 10 nm. From the results of TG analysis in Figure 2b, the mass ratio of coated lipid bilayer was calculated as 25.8%. The hydrodynamic diameter and zeta potential of dHMSN were 186.4 ± 5.0 nm and -19.9 ± 1.6 mV respectively, while the diameter of dHMLB increased to 243.0 ± 11.3 nm and zeta potential changed to -11.7 ± 2.0 mV which was close to the zeta potential of liposome (-8.5 ± 1.5 mV, not shown in the figure), both indicating the lipid bilayer coating structure (Figure 2c). It's well known that lipid coating could evidently increase the stability of dHMSN in PBS [42]. In Figure S3, compared with the instable dHMSN solution, which easily precipitated in short time, dHMLB was well dispersed in PBS and could keep good stability after loading drug. *In vitro* stability of dHMLB was further performed in FBS at room temperature and 37°C (Figure 2d). Biocompatibility of dHMLB was evaluated by *in vitro* cell viability compared with dHMSN. dHMLB exhibited significant low cytotoxicity on L929 cells at various concentrations compared with that of dHMSN, especially at high concentration of 1000 and 5000 μg/mL (Figure 2e). Hemolysis assay demonstrated that dHMSN and dHMLB were not likely to induce hemolysis as shown in Figure 2f. Therefore, lipid coating can greatly increase the safety and stability of dHMSN.

Drug loading and *in vitro* release profiles

The structure of HMSN can promote loading capability of drugs with different properties to exert synergistic effects. From the characterizations above, dHMSN have exhibited adjustable core/shell thickness and large surface area, which provided a great capacity in various agents co-encapsulation. In this study, DOX, ATRA and IL-2 were selected as therapeutic agents for combinational treatment in melanoma model. dHMSN with core size of 70 nm and shell thickness of 55 nm was chosen (Figure 1a-ii) to achieve a more rational and stable co-loading of ATRA and DOX. Amino-modified dHMSN

(NH_2-dHMSN) was fabricated to enhance the loading capacity of ATRA, of which the DLE increased from 10.3% to 48.9%. The biodegradability was not affected after modification (Figure S4). In Figure 3a, a new peak appearing at 2920 cm^{-1} which corresponded to -CH- group of aminopropyl from APTES molecules, and the purple color emerging in ninhydrine reaction (the inset of Figure 3a) both confirmed the success of amino modification on dHMSN. The DLE of ATRA and DOX in dHMSN could reach 48.9 ± 7.8% and 23.1 ± 3.5% respectively, and the absorbed IL-2 after incubation could reach 90%. The more ATRA or DOX was fed, the more amount of drugs was loaded within a certain range. However, too much loaded ATRA could influence the followed encapsulation of DOX and stability of nanoparticles. So the appropriate feeding mass ratio of dHMSN/ATRA and dHMSN/DOX was finally explored to be both 2/1 to achieve a rational co-encapsulation of drugs and good stability. In the result of TG analysis of drug-loaded dHMSN (Figure 3b), ATRA and DOX could be co-loaded in the nanoparticles almost at the ratio of 3/1 as the expectation of administration [23]. *In vitro* drug release was conducted in PBS with pH 7.4 and 6.8, respectively presenting the physiological condition and tumor microenvironment. dHMLB displayed the controlled release behavior of each loaded drug (Figure S5). The slightly increased release kinetics at decreased pH may be partially attributed to the increased acidity, which could weaken electronic interaction between amine group of dHMSN and ATRA, as well as between silanol group and DOX. In addition, it has been confirmed that acid condition can destabilize supported lipid bilayers of porous nanoparticles and make encapsulated cargo diffuse out of the nanoporous core [43]. The formulated dHMLB provided an excellent platform for co-encapsulating chemotherapeutics and immune agent with controlled release behaviors, to realize subsequent synergistic antitumor efficiency.

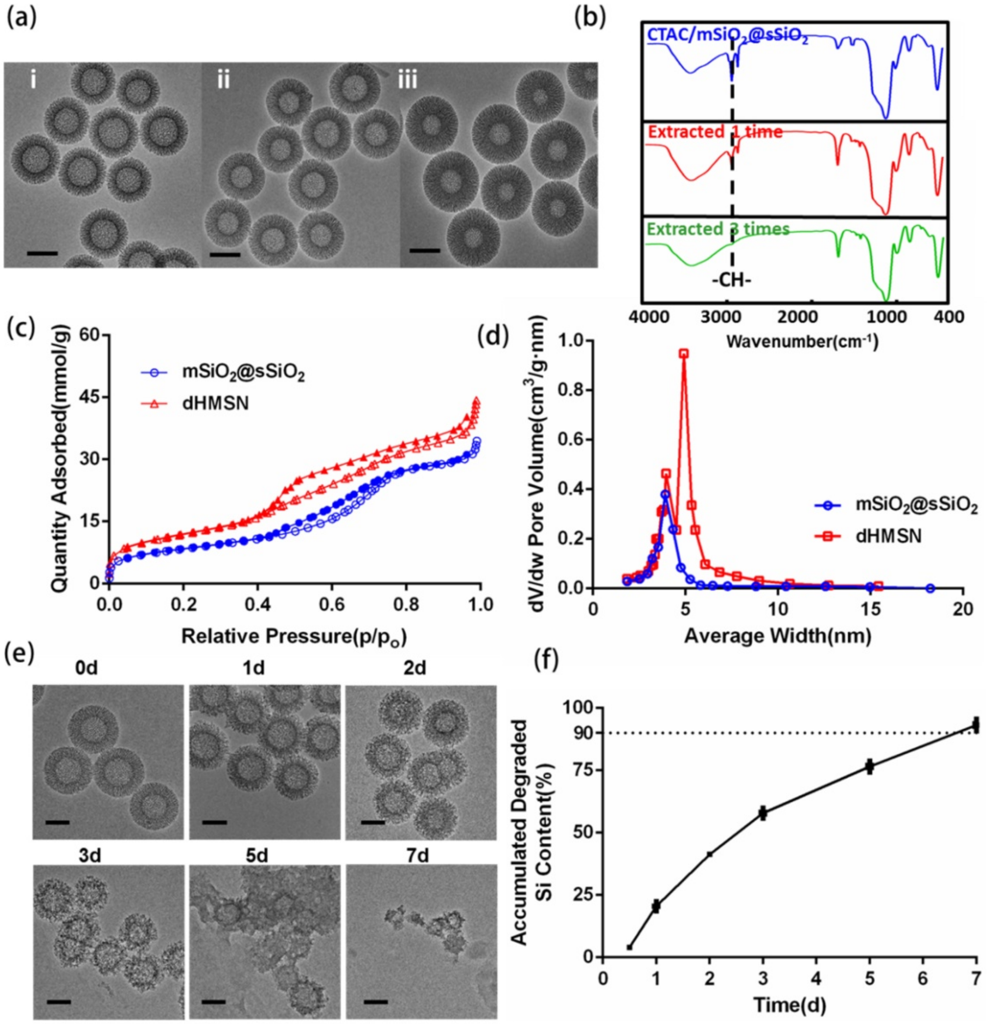

Figure 1. Characterizations of dHMSN. (a) TEM images of dHMSN with different core size and shell thickness, (i) core: 100 nm, shell: 40 nm, (ii) core: 70 nm, shell: 55 nm, (iii) core: 50 nm, shell: 65 nm. (b) FT-IR spectra of CTAC/$mSiO_2@sSiO_2$ before and after extracted with HCl-ethanol solution. (c) Nitrogen adsorption-desorption isotherms and (d) Pore size distribution of $mSiO_2@sSiO_2$ and dHMSN. (e) TEM images of dHMSN at different degradation intervals in PBS at 37°C. (f) *In vitro* biodegradation profile of dHMSN in PBS at 37°C. All scale bars in TEM images are 100 nm.

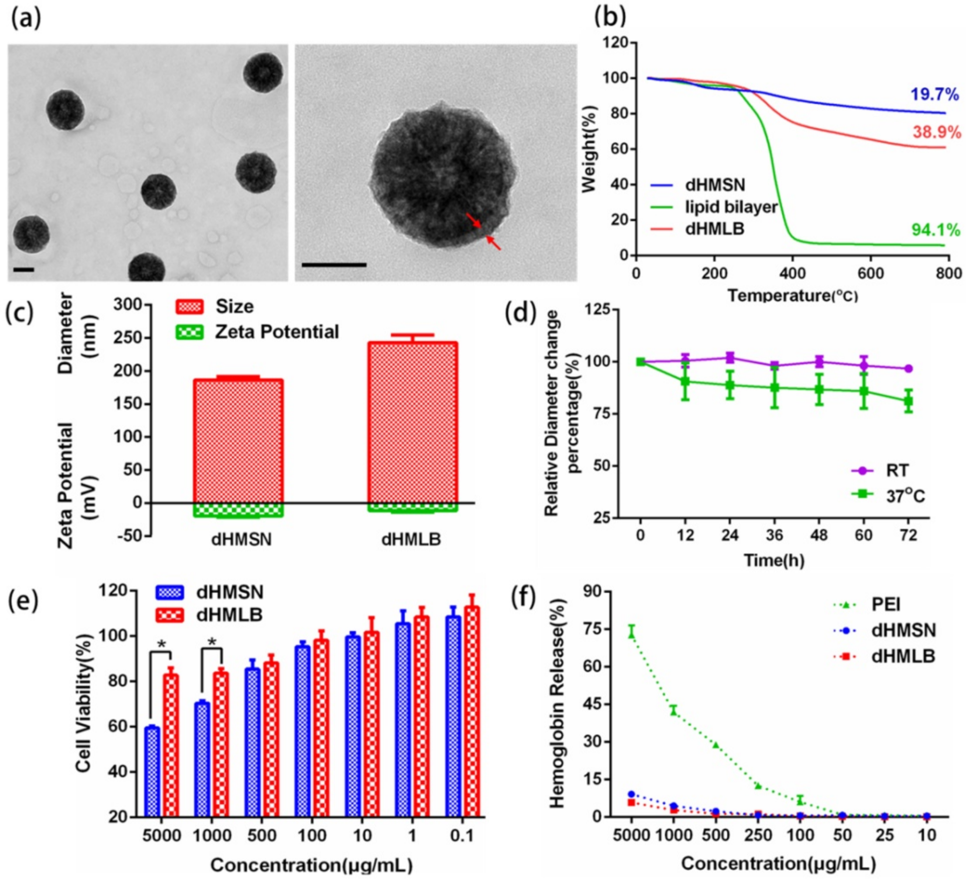

Figure 2. Characterizations of dHMLB. (a) TEM images of dHMLB. (b) TG curves of dHMSN, lipid bilayer and dHMLB. (c) Hydrodynamic diameter and zeta potential of dHMSN and dHMLB measured by DLS in PBS. (d) *In vitro* stability of dHMLB in FBS at room temperature (RT) and 37°C. (e) *In vitro* cytotoxicity of dHMSN and dHMLB against L929 cells after treatment for 24 h. (f) Hemolysis assay of dHMSN and dHMLB incubated with RBCs for 4 h at 37°C. All scale bars in TEM images are 100 nm.

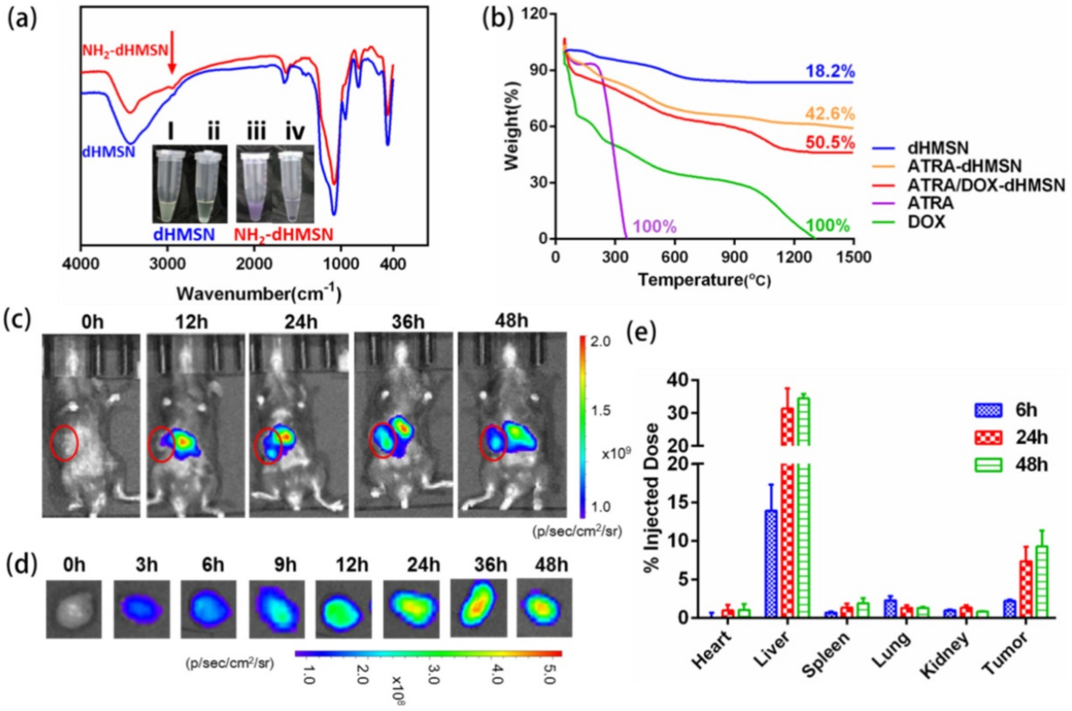

Figure 3. Drug loading of dHMSN and Biodistribution of dHMLB. (a) FT-IR spectra of amino modification of dHMSN. Inset : ninhydrine reaction before and after amino modification. (i), (iii) the suspension of dHMSN and NH_2-dHMSN. (ii), (iv) the supernatant of dHMSN and NH_2-dHMSN. (b) TG curves of free drugs, dHMSN and drug-loaded dHMSN. (c) *In vivo* imaging of mice and (d) *ex vivo* imaging of tumor from B16F10 tumor-bearing C57/BL6 mice which were *i.v.* injected with Cy5-loaded dHMLB. (e) Biodistribution of Si at 6 h, 24 h and 48 h post injection of dHMLB.

Table 1. Pharmacokinetic parameters of free ATRA, DOX, IL-2 and A/D/I-dHMLB in rats after *i.v.* injection at equivalent dose of all agents.

Parameters	unit	ATRA	dHMLB	unit	DOX	dHMLB	unit	IL-2	dHMLB
Dose	mg/kg	15.00	15.00	mg/kg	5.00	5.00	μg/kg	2.50	2.50
AUC_{0-t}	mg/L·h	22.32 ± 1.04	38.85 ± 5.12	mg/L·h	1.04 ± 0.52	5.38 ± 0.06	ng/L·h	197.28 ± 30.93	434.14 ± 89.23
$AUC_{0-\infty}$	mg/L·h	22.60 ± 1.13	40.40 ± 6.00	mg/L·h	1.17 ± 0.53	6.08 ± 0.49	ng/L·h	204.89 ± 21.81	439.74 ± 89.3
MRT_{0-t}	h	1.90 ± 0.05	4.80 ± 0.59	h	6.88 ± 0.19	20.64 ± 1.04	h	1.04 ± 0.09	2.39 ± 0.15
$MRT_{0-\infty}$	h	2.00 ± 0.09	5.77 ± 1.35	h	14.90 ± 5.75	31.11 ± 2.61	h	1.62 ± 1.02	2.54 ± 0.22
$t_{1/2}$	h	1.29 ± 0.09	4.91 ± 0.99	h	9.32 ± 5.04	24.34 ± 6.29	h	0.77 ± 0.16	1.98 ± 0.12
CL	L/h/kg	0.67 ± 0.03	0.38 ± 0.06	L/h/kg	4.84 ± 1.91	0.83 ± 0.06	L/h/kg	12.29 ± 1.23	5.86 ± 1.29
C_{max}	mg/L	8.65 ± 0.49	7.27 ± 0.51	mg/L	0.33 ± 0.18	0.36 ± 0.05	ng/L	114.83 ± 18.03	162.06 ± 23.81
T_{max}	h	0.50	0.50	h	0.50	0.50	h	0.50	0.50

Biodistribution and pharmacokinetic study

To evaluate the biodistribution of dHMLB in tumor-bearing mice, Cy5-loaded dHMLB was *i.v.* injected and mice were imaged by IVIS. As seen in Figure 3c, nanoparticles demonstrated gradual distribution in tumor and the strongest fluorescence presented at 36 h, which was in accordance with *ex vivo* imaging of tumor (Figure 3d). The tumor exhibited the lasting florescence, which indicated the long circulation property and enhanced permeability and retention effect of nanoparticles in tumor site. The biodistribution of dHMLB was also quantitatively performed at 6 h, 24 h and 48 h post injection *via* ICP-MS analysis (Figure 3e). It showed 2.21 ± 0.17% of Si accumulation in tumor at 6 h and increased to 7.32 ± 1.91% and 9.25 ± 2.05% at 24 h and 48 h, respectively. dHMLB showed the most accumulation of Si in liver at 6 h, 24 h or 48 h, and only less than 3% of the total injected dose was presented in the heart, spleen, lung and kidney.

ATRA, which has poor aqueous solubility, physicochemical instability and unfavorable pharmacokinetic behavior, is always quickly metabolized in the body [44, 45]. IL-2, a kind of soluble protein cytokine, is easily degraded with short half-life in plasma [46]. Herein, *in vivo* behavior of drug-loaded dHMLB was investigated. Pharmacokinetic study of free agents and A/D/I-dHMLB were shown in Figure S6 and pharmacokinetic parameters were summarized in Table 1. Compared with free ATRA, DOX, and IL-2, A/D/I-dHMLB exhibited better pharmacokinetic profiles. Nanoparticles demonstrated 1.79-, 5.20-, and 2.15-fold area under concentration (AUC) of free ATRA, DOX and IL-2, respectively. Moreover, half-life ($t_{1/2}$) of ATRA, DOX and IL-2 in A/D/I-dHMLB was 4.91 ± 0.99 h, 24.34 ± 6.29 h and 1.98 ± 0.12 h, respectively, which were up to 3.81-, 2.61- and 2.57-fold of free agents. The prolonged drug circulation benefiting from dHMLB could facilitate the delivery and accumulation of drugs in tumor, thus enhancing the antitumor efficacy.

Evaluation of antitumor activity in B16F10 tumor model

B16F10 melanoma is a kind of malignant tumor with high metastatic possibility and poor prognosis. We exploited this tumor model to evaluate the antitumor effect of drug-loaded dHMLB in C57BL/6 mice. Considering that DOX acted as the main chemotherapeutic agent of inducing tumor cell death in this combinational therapy, the dosage optimization of DOX was firstly explored. The common injection dosage of DOX in chemotherapy was 5 mg/kg, so series of dosage were applied as 0.5, 1, 2.5, and 5 mg/kg in the first exploration. According to previous report [23], ATRA and DOX can develop good synergistic antitumor effect at the mass ratio of 3/1. A/D-dHMLB with or without IL-2 co-encapsulation was evaluated here to investigate the synergistic effect from chemo-immunotherapy and the dosage of IL-2 was fixed as 2.5 μg/kg as previously reported [38]. From Figure S7-i, compared with others, A/D/I-dHMLB-2.5, A/D-dHMLB-5 and A/D/I-dHMLB-5 exhibited significant tumor growth inhibition but no significant difference among them. It seemed that ATRA/DOX combined with IL-2 in dHMLB at 2.5 mg/kg could develop good synergy effect and almost exert the similar inhibition effect with that of 5 mg/kg, which indicated the indispensable role of IL-2 in this combinational therapy. The inhibition effect of A/D/I-dHMLB at 2.5 mg/kg was further compared with free DOX, free drugs combination and A/D/I-dHMLB at 5 mg/kg in the second exploration (Figure S7-ii), which showed similar inhibition activity with the precedent exploration. Lower dose of chemotherapeutic agent means lower toxicity and greater potential of immune system modulation. Therefore, in the followed animal experiments, the dosage of DOX was determined as 2.5 mg/kg, and that of ATRA was 7.5 mg/kg, accordingly. To further evaluate the antitumor effect from drug-loaded dHMLB, tumor-bearing mice were treated with DOX (D), DOX+IL-2 (D/I), ATRA+DOX (A/D), ATRA+DOX+IL-2 (A/D/I), and corresponding drug-loaded dHMLB, respectively. As Figure 4a and 4b shown, A/D/I-dHMLB exhibited the most effective tumor growth inhibition among all the groups and also significant synergistic antitumor effect compared with D/I-dHMLB and A/D-dHMLB ($p < 0.05$). The tumor weight (Figure 4c) and inhibitory rate (Figure 4d) also showed the similar trend. A/D/I-dHMLB exhibited much higher tumor inhibitory rate of 84.8 ± 13.0%, compared with that of D, D/I, A/D, A/D/I, D-dHMLB, D/I-dHMLB and A/D-dHMLB which were 17.1 ± 12.4%, 37.1 ± 17.8%, 46.7 ± 25.4%, 52.4 ± 18.5%, 42.9 ± 14.8%, 58.8 ± 22.8% and 61.7 ± 23.1%, respectively. Moreover, no significant body weight change was observed in all treatment groups (Figure 4e). In H&E staining results (Figure 4f), tumor treated with A/D/I-dHMLB showed the most obvious necrosis area. No apparent lung metastatic lesion was found in all groups except for saline. All these results demonstrated that the nanoparticles co-encapsulating tumor microenvironment modulator, chemotherapeutic and immune agent (A/D/I-dHMLB) could realize better synergy effects on inhibiting tumor growth compared with that of any two therapeutic agents co-loaded nanoparticles (A/D-dHMLB and D/I-dHMLB).

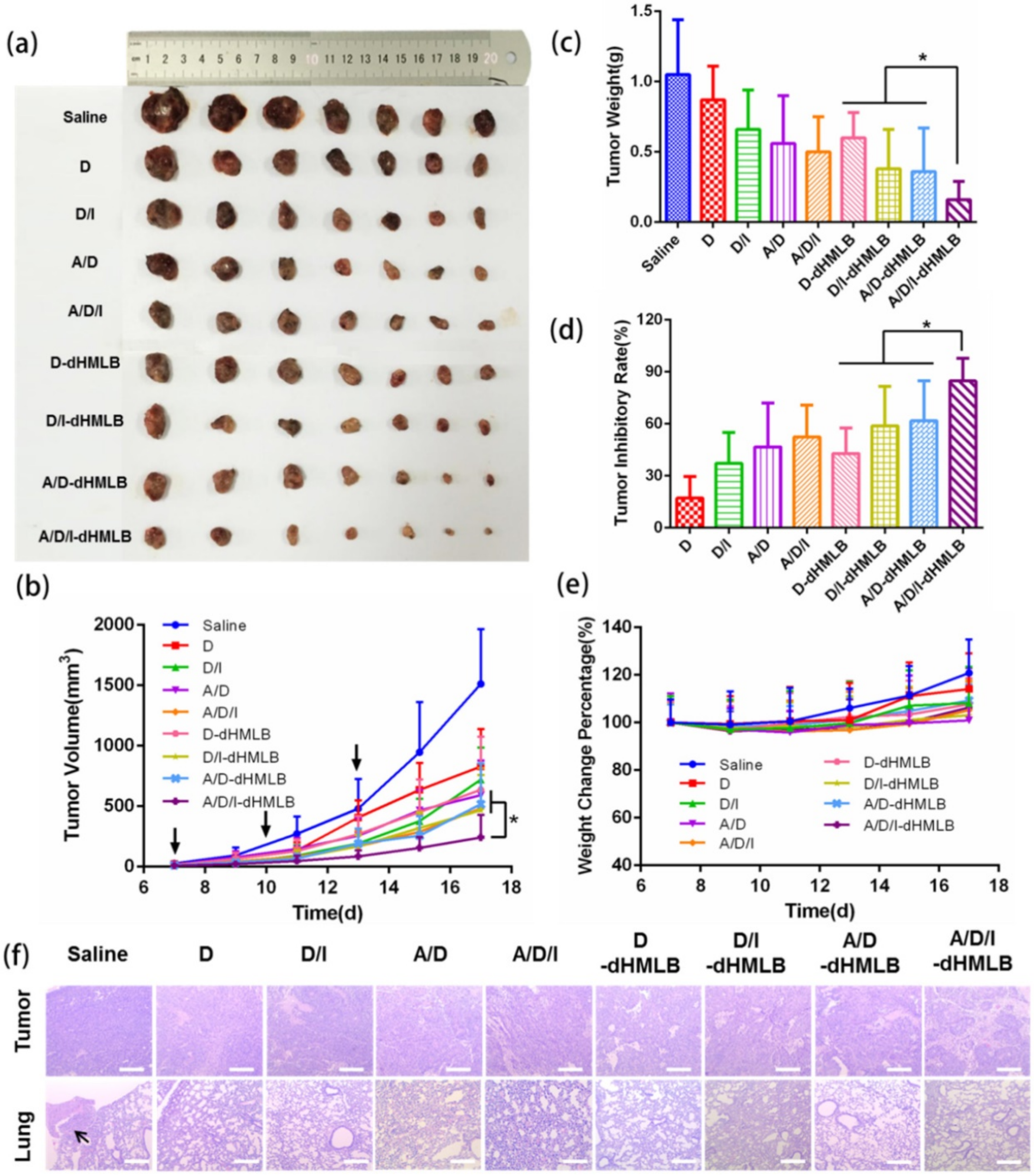

Figure 4. Antitumor activity of different formulations in B16F10 tumor model. (a, c) Mice were sacrificed and tumors were harvested on 18th day for (a) image and (c) weight. (b) Tumor growth curves. (d) Tumor inhibitory rate of different groups compared with saline. (e) Body weight changes of tumor-bearing mice. (f) Representative H&E staining sections in tumor and lung excised from tumor-bearing mice (Magnification: 40×). The arrow points the metastatic nodule. All scale bars are 625 μm.

Evaluation of tumor metastasis inhibition

B16F10 melanoma has high potential of metastasis in lung. As presented in subcutaneous tumor model above, whether drug-loaded dHMLB could inhibit metastasis was not sufficiently exhibited in H&E staining results of lung. Herein, metastatic inhibition was further investigated in B16F10 lung metastasis experiment. The counted pulmonary metastatic nodules were presented in Figure 5a, which showed evidently smaller number in A/D/I-dHMLB group (60 ± 6) compared with saline (184 ± 23), A/D/I (120 ± 12), D-dHMLB (121 ± 11), D/I-dHMLB (110 ± 13) and A/D-dHMLB (106 ± 9) ($p < 0.001$). The similar trend was also seen in the results of metastatic inhibitory rate (Figure 5b) and lung/body weight ratio (Figure 5c). Representative lung images and H&E staining of lung nodules were respectively shown in Figure 5d and 5e. A/D/I-dHMLB treated group showed the decreased area of metastasis, which was further confirmed by immunohistochemical staining of S100, a common melanoma marker. However, livers and kidneys in all groups did not show any metastatic foci (Figure 5e). The images of lungs, livers and kidneys were displayed in Figure S8. Similar to the therapeutic trend in subcutaneous tumor model, A/D/I-dHMLB induced the enhanced metastasis inhibition compared with D/I-dHMLB and A/D-dHMLB. In this drug delivery system, immune response activated by A/D/I-dHMLB and the reported anti-metastasis property of ATRA were supposed to contribute to anti-metastasis effect [47]. More comprehensive studies are needed to investigate the anti-metastatic mechanism in the future. Anyway, this drug co-delivery system was still supposed to be a promising combinational strategy against melanoma metastasis.

In vivo systematic toxicity evaluation

Safety of formulation is an essential indicator for drug delivery *in vivo*. After treatment of different formulations, systematic toxicity evaluation was conducted by assessing serum chemistry levels and histopathology. The levels of ALT, AST and BUN were shown in the normal range (Figure 6a). H&E staining of major organs including heart, liver, spleen, lung and kidney of saline and A/D/I-dHMLB treated groups were presented in Figure 6b (others in Figure S9, lung shown in Figure 4f). No apparent lesion was shown in heart, liver, spleen and kidney. No cardiac pathological change from free DOX treated group may be attributed to the low dosage administration. Therefore, drug-loaded dHMLB could be applied as a safe formulation for *i.v.* administration.

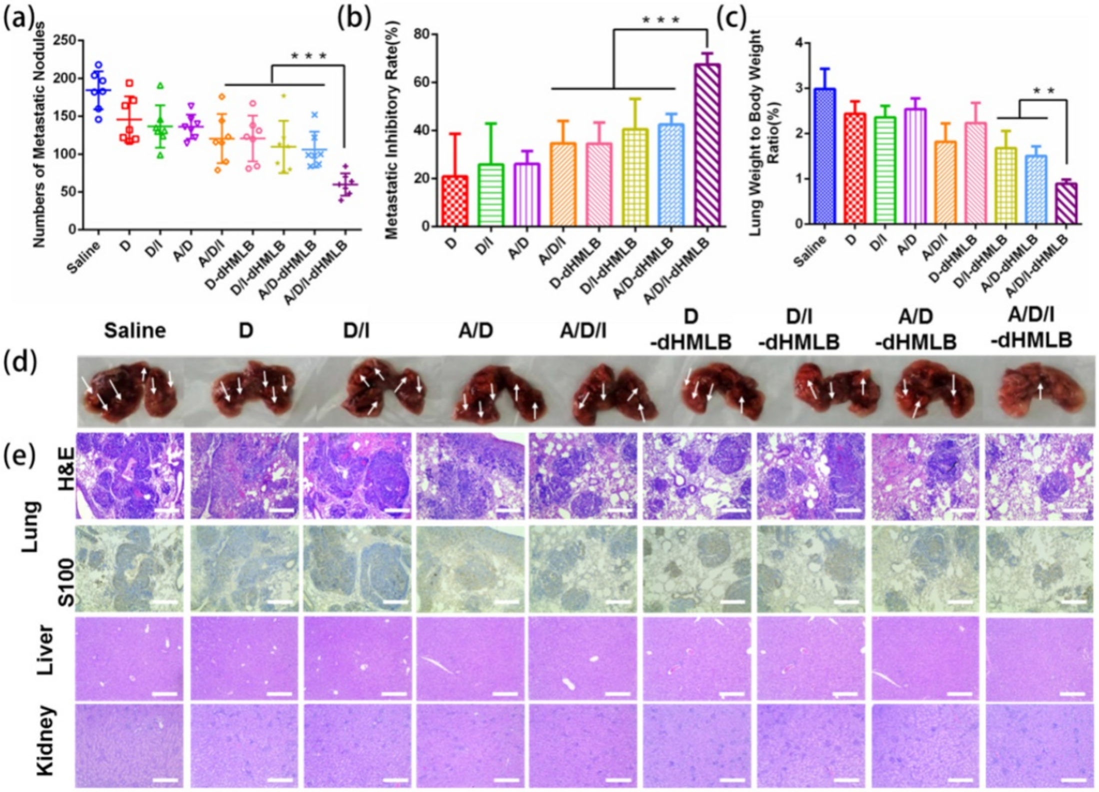

Figure 5. Metastasis inhibition of different formulations in B16F10 metastatic tumor model. (a) Number of metastatic nodules. (b) Metastatic inhibitory rate in each group was calculated compared with saline. (c) Lung/body weight ratio. (d) Lungs were harvested for image. (e) Representative H&E staining and S100 immunohistochemistry of lung, and representative H&E staining sections of liver and kidney (Magnification: 100×). All scale bars are 250 μm.

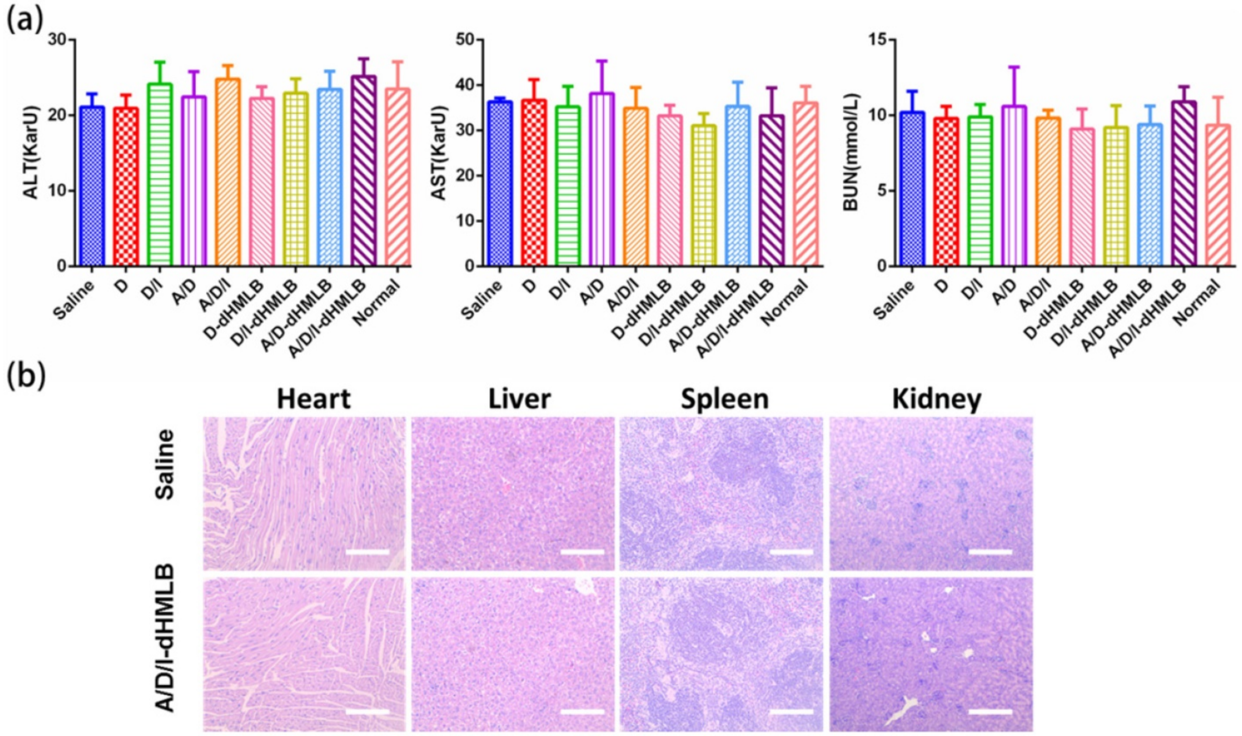

Figure 6. Evaluation of systematic toxicity of different formulations. (a) Serum chemistry levels including ALT, AST and BUN in each group compared with normal levels. (b) Organs of saline and A/D/I-dHMLB treated groups were excised for H&E staining (Magnification: 100×). All scale bars are 250 μm.

Assessment of immune response in tumor microenvironment

The favorable performance of A/D/I-dHMLB in inhibiting tumor growth and metastasis has been fully demonstrated above, and its synergy mechanism was thus investigated. Immune system plays an important role in tumor treatment, while immunosuppression in tumor microenvironment impedes the efficiency of cancer immunotherapy. Herein, assessment of immune response was focused on tumor microenvironment. ATRA has been found to be capable of differentiating MDSCs into DCs and others, thus relieving MDSC-induced inhibition on T cell functions. In addition, ICD effect induced by low dosage of DOX also contributed to the stimulation of immune response by enhancing DC maturation and antigen presentation. So MDSC and DC populations in tumor after treatment were first analyzed (Figure 7). In Figure 7a, the combination of ATRA can significantly reduce MDSC population in free drugs or drug-loaded dHMLB, which indicated the important role of ATRA in depleting MDSCs. The number of MDSC decreased 1.8- and 1.9-fold in free A/D and A/D/I, respectively compared with that of saline, while A/D-dHMLB and A/D/I-dHMLB demonstrated 2.4- and 2.7-fold decrease, respectively ($p < 0.05$). In Figure 7b and 7c, A/D-dHMLB and A/D/I-dHMLB significantly increased DC population and also promoted DC maturation compared with that of saline and free drug combinations ($p < 0.05$). The number of DC and mature DC in A/D/I-dHMLB increased 14.1-fold and 14.3-fold, respectively compared with that of saline. These may be attributed to the synergistic effect of ATRA and DOX in modulating tumor microenvironment. The promotion of DC maturation could be beneficial to the stimulation of immune system for inducing tumor-specific immune response.

Activation of CTL-specific killing on tumor cells is an essential strategy to improve antitumor immune response. In this study, IL-2 in the combination therapy could facilitate T lymphocytes proliferation and extend survival time [26, 48]. Thus, to evaluate the function of IL-2 on T lymphocytes, $CD8^+$ T cells were investigated here. As shown in Figure 8a and 8b, the number of $CD8^+$ T cell increased 3.41-, 3.99-, 5.78-fold and number of activated $CD8^+$ T cell increased 2.49-, 2.90-, 3.93-fold in D/I-dHMLB, A/D-dHMLB and A/D/I-dHMLB compared with that of saline, respectively. The activated T lymphocytes can promote effective tumor killing of T cells. Furthermore, the combination of ATRA in dHMLB also exhibited synergistic effect from the improved $CD8^+$ T cells population. It may be attributed that ATRA could relieve the suppression on T lymphocytes function and thus enhance antitumor immunity. $CD4^+$ T cells were also assessed and A/D/I-dHMLB showed 6.33-fold increase compared with that of saline (Figure S10). Besides, IFN-γ producing CD8+ T cells were analyzed (Figure 8c). Different from the weak expression in saline, combinational treatment with dHMLB significantly increased the number of IFN-γ producing CD8+ T cells, especially in A/D/I-dHMLB group (33.3-fold). This enhancement was also evidenced in CD8+ and IFN-γ+ immunofluorescence assay (Figure 8d). IFN-γ secretion in tumor and blood was also detected and analyzed in Figure 9a and 9b. Corresponding to the previous results, the secretion of IFN-γ in tumor and plasma treated with A/D/I-dHMLB increased near 6- and 11-fold respectively compared with that of saline. IFN-γ, a kind of T-helper I (Th1) cells-derived cytokine, plays a critical role in regulating T cells, B cells, macrophages and NK cells[49], as well as involving in antigen presentation through major histocompatibility complex class I and II molecule[50]. The enhanced secretion of IFN-γ is favorable for inducing antitumor immune response. Moreover, IL-2 can also strengthen the function of NK cells [51] and it was analyzed in Figure 9c. A/D/I-dHMLB showed 9.28- and 1.68-fold increase compared with that of saline and A/D/I respectively, indicating the activation of innate immune system.

Other cytokines such as IL-12p70, IL-10, TNF-α and TGF-β, which are all involved in immune response in tumor microenvironment, were detected and analyzed. IL-12 acted as a T cell stimulating factor to facilitate T cell growth and contributed to the production of IFN-γ, thus enhancing Th1-type immune response [52]. TNF-α, a kind of inflammatory reaction related cytokine, is capable of inducing tumor cells death and related to CD8+ T cell stimulation[53]. From the results in Figure 9d and 9e, levels of IL-12p70 and TNF-α in A/D/I-dHMLB both increased about 3-fold compared with that of saline. IL-10 and TGF-β, both inhibitory cytokines in innate and adaptive immunity, dropped over 6- and 3-fold, respectively in A/D/I-dHMLB (Figure 9f and 9g). The actual detected concentrations of cytokines were displayed in Figure S11. These changed cytokines secretion could strengthen the communication

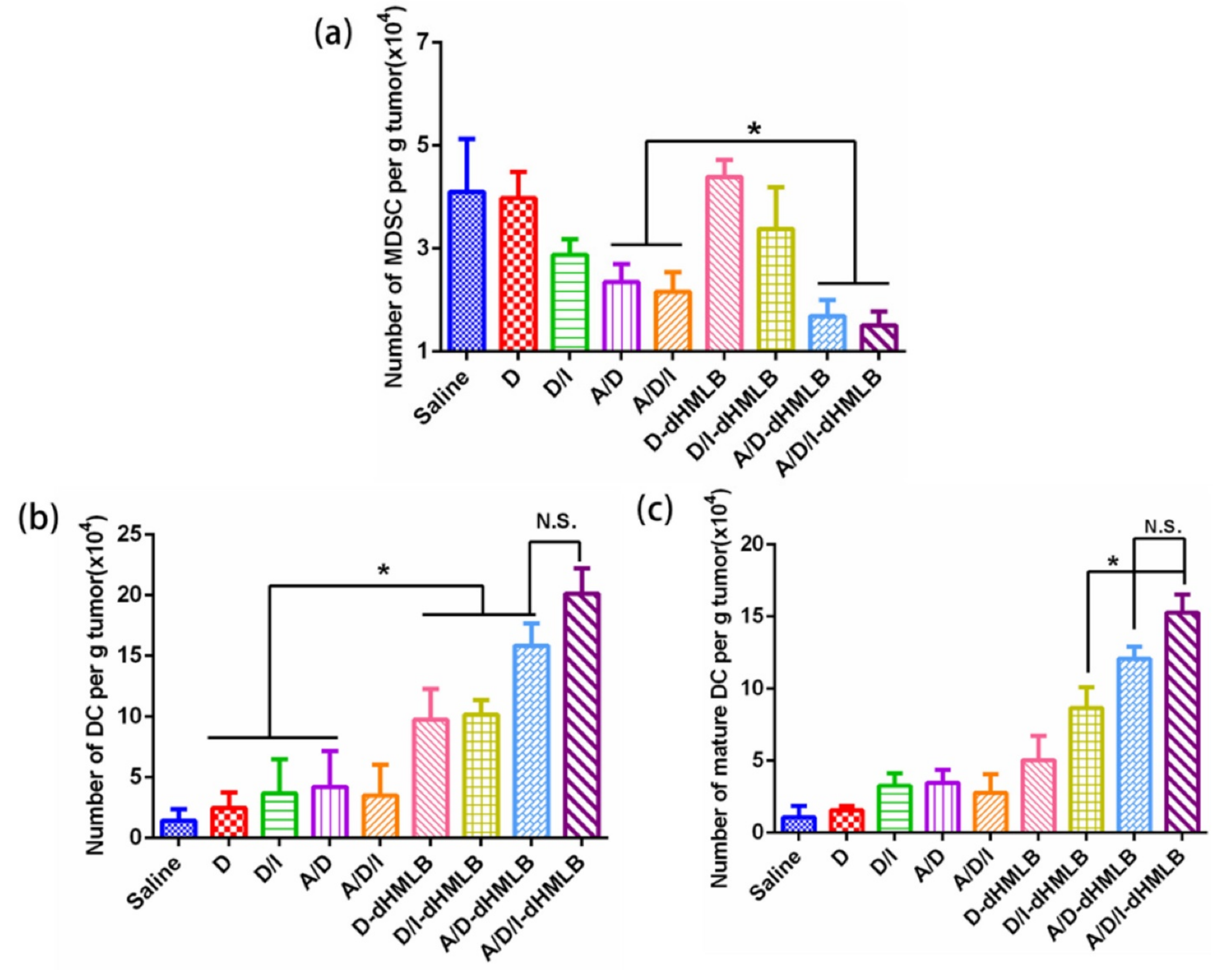

Figure 7. Decrease of MDSC and maturation of DC in tumor. Number of (a) MDSC (CD11b+Gr-1+), (b) DC (CD11c+) and (c) mature DC (CD11c+CD86+) per gram of tumor mass.

between immune cells and tumor cells, thus creating an activated immune microenvironment. In addition, immunostimulatory effect induced by the plain HMSN has been reported in recent studies [54, 55]. HMSN loaded with tumor antigen showed adjuvant activity to inhibit the development of tumor by promoting Th1 and Th2 antitumor immunity and increasing effector memory CD4$^+$ and CD8$^+$ T cell populations in immune organs. In order to check the possible immunomodulation of dHMSN, the immune cells and cytokines secretion were also assessed in tumor and blood after *i.v.* injected with plain dHMLB (Figure S12). It was found that dHMLB had no obvious modulation on the secretion of immune cytokines, but could slightly promote the maturation of DCs and proliferation of T cells. It seemed that dHMSN worked as not only an excellent vehicle, but also a potential immunoregulatory agent in this drug delivery system.

As demonstrated above, we figured out the synergy mechanism of DOX, ATRA and IL-2 co-delivered by dHMLB in tumor microenvironment, which was illustrated in Scheme 1. DOX exerted the main chemotherapeutic killing on tumor cells. And apoptotic tumor cells could release tumor antigens, which could be taken up by DCs and presented to T cells. Moreover, immunosuppressive MDSCs in tumor could be differentiated into DCs by ATRA, thus restoring the function of T lymphocytes. At the same time, IL-2 facilitated the activation of CTLs and NK cells in tumor microenvironment. Furthermore, the combination of DOX, ATRA and IL-2 promoted the secretion of immunomodulating cytokines, like IFN-γ and IL-12. In a word, the enhanced antitumor immunity could be achieved by synergistic effect of A/D/I-dHMLB with immunosuppressive cells depletion and immune effector cells activation in tumor microenvironment.

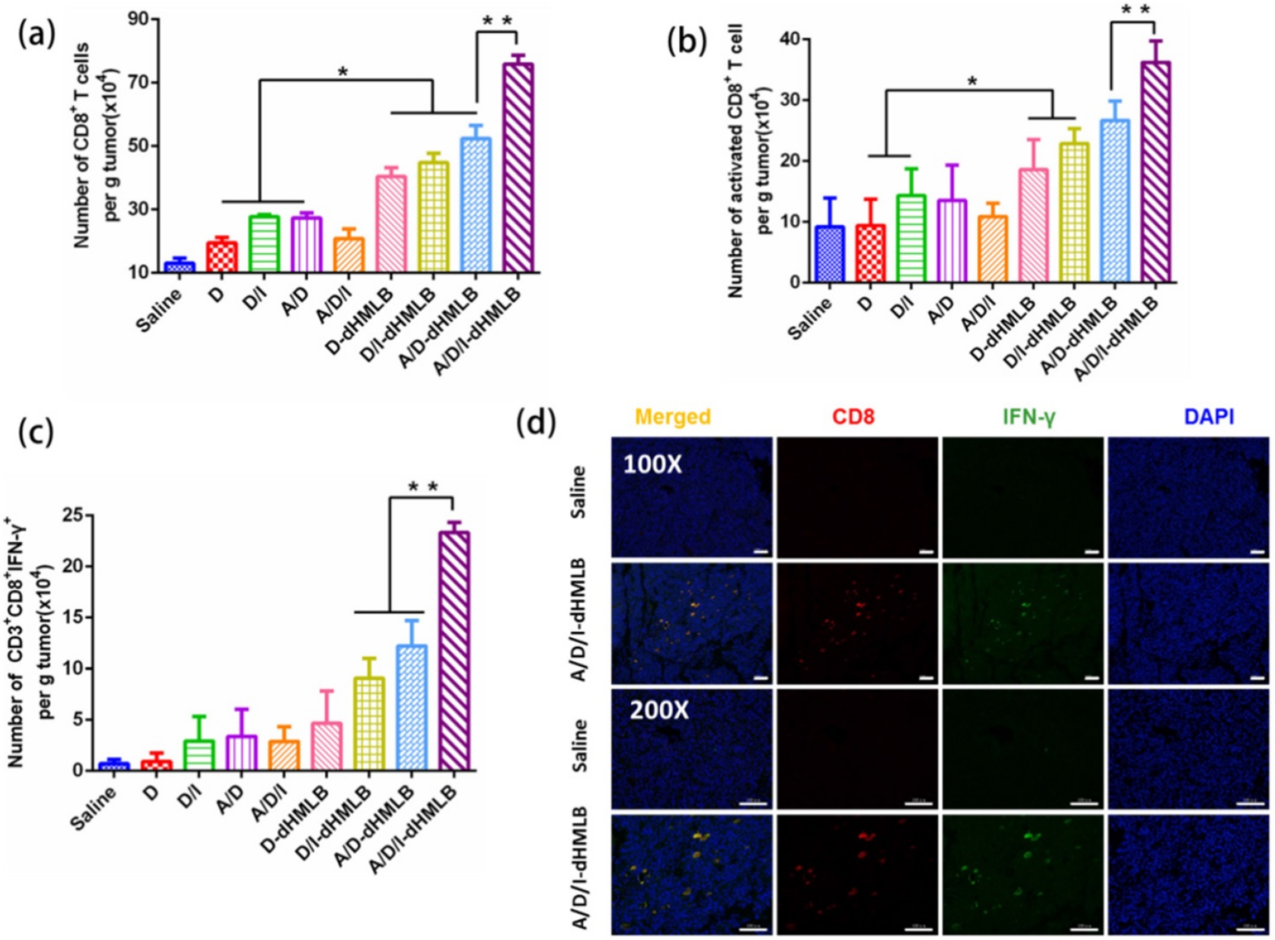

Figure 8. Immune response analysis. (a-c) Number of CD8$^+$ T cells (CD3$^+$CD8$^+$), activated CD8$^+$ T cells (CD3$^+$CD8$^+$CD69$^+$), CD3$^+$CD8$^+$IFN-γ$^+$ cells per gram of tumor. (d) CD8$^+$ and IFN-γ$^+$ immunofluorescence assay. All scale bars are 100 μm.

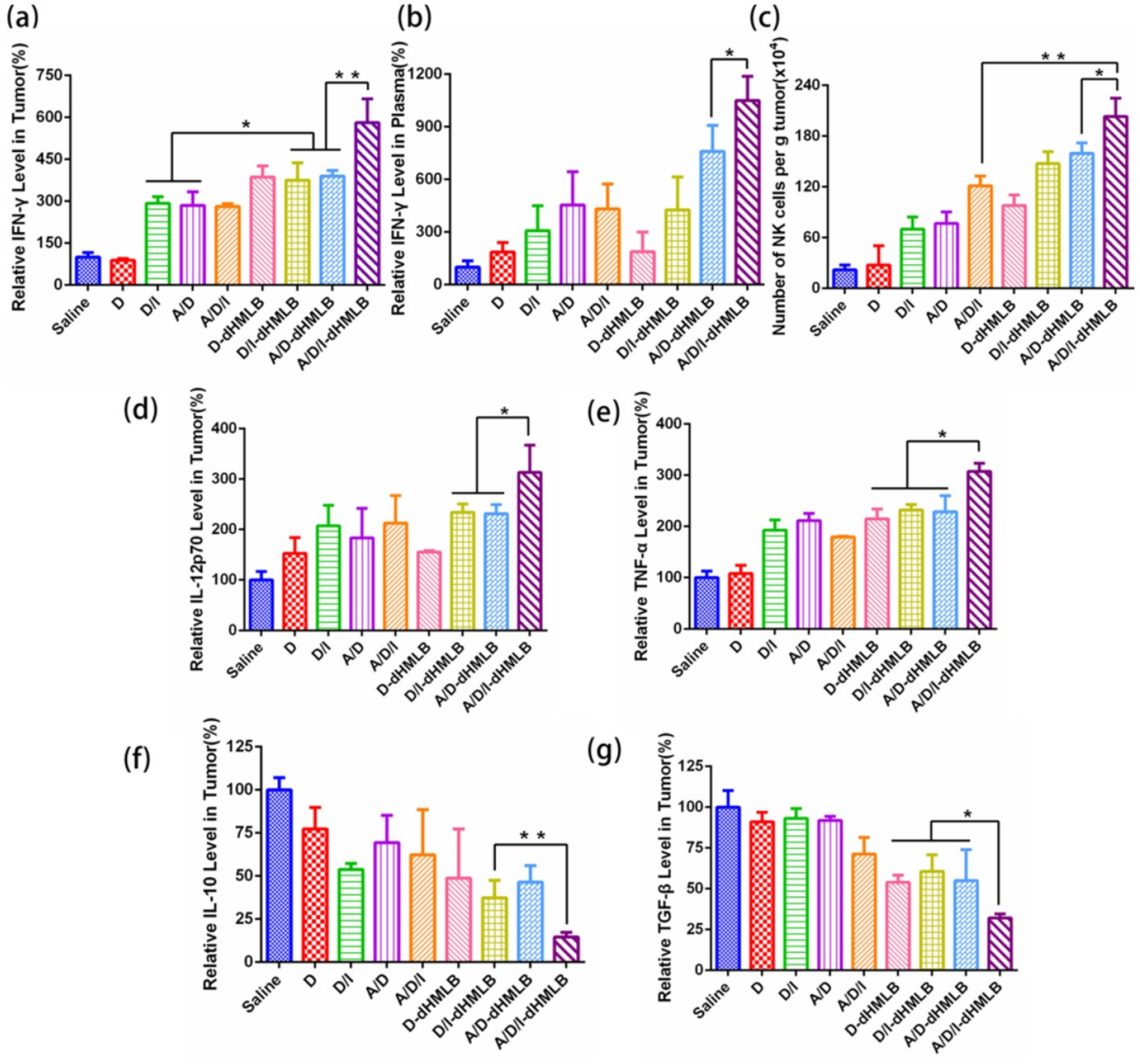

Figure 9. Immune response and cytokine analysis. (a, b) Relative IFN-γ level in tumor and plasma. (c) Number of NK cells (CD3$^-$NK1.1$^+$) per gram of tumor. (d-g) Relative levels of IL-12p70, TNF-α, IL-10 and TGF-β in tumor.

Conclusion

In this study, lipid-coated biodegradable hollow mesoporous silica nanoparticle was constructed to realize co-delivery of three agents and subsequent chemo-immunotherapeutic antitumor effects. The nanoparticles possessed excellent encapsulation capacity, satisfactory stability, favorable biodistribution and low systemic toxicity. More importantly, the nanoparticle-mediated combinational therapy can fully develop the synergy effects with significant inhibition on tumor growth and metastasis. This is benefited from induction of tumor apoptosis by chemotherapeutic drug DOX, modulation of immunosuppressive tumor microenvironment by ATRA and enhancement of antitumor immunity by cytokine IL-2. Facing the complexity and variability of tumor microenvironment, multiple mechanisms involved therapies are recommended. Chemo-immunotherapy as one of the feasible strategies has drawn much attention in cancer treatment. This drug delivery system provides a nanoplatform for multidrug co-encapsulation and holds great potential in cancer combinational therapy.

Acknowledgements

This work was supported by the National Natural Science Foundation of China (81373360 and 81673374); Fundamental Research Funds for the Central Universities (2015ZDTD048 and 2016YXMS138). We thank the Analytical and Testing

Center of HUST for performing TEM, FT-IR, TGA and ICP-MS.

Supplementary Material

Materials and reagents, cells and animals, supplemented figures. http://www.thno.org/v07p3276s1.pdf

Competing Interests

The authors have declared that no competing interest exists.

References

1. Da Silva CG, Rueda F, Löwik CW, Ossendorp F, Cruz LJ. Combinatorial prospects of nano-targeted chemoimmunotherapy. Biomaterials. 2016; 83: 308-20.
2. Zou W. Immunosuppressive networks in the tumour environment and their therapeutic relevance. Nat Rev Cancer. 2005; 5: 263-74.
3. Galluzzi L, Senovilla L, Zitvogel L, Kroemer G. The secret ally: immunostimulation by anticancer drugs. Nat Rev Drug Discov. 2012; 11: 215-33.
4. Pfirschke C, Engblom C, Rickelt S, Cortez-Retamozo V, Garris C, Pucci F, et al. Immunogenic chemotherapy sensitizes tumors to checkpoint blockade therapy. Immunity. 2016; 44: 343-54.
5. Whiteside TL. The tumor microenvironment and its role in promoting tumor growth. Oncogene. 2008; 27: 5904-12.
6. Krysko DV, Garg AD, Kaczmarek A, Krysko O, Agostinis P, Vandenabeele P. Immunogenic cell death and DAMPs in cancer therapy. Nat Rev Cancer. 2012; 12: 860-75.
7. Zhao X, Yang K, Zhao R, Ji T, Wang X, Yang X, et al. Inducing enhanced immunogenic cell death with nanocarrier-based drug delivery systems for pancreatic cancer therapy. Biomaterials. 2016; 102: 187-97.
8. Kapadia CH, Perry JL, Tian S, Luft JC, DeSimone JM. Nanoparticulate immunotherapy for cancer. J Control Release. 2015; 219: 167-80.
9. Zhang L, Dermawan K, Jin M, Liu R, Zheng H, Xu L, et al. Differential impairment of regulatory T cells rather than effector T cells by paclitaxel-based chemotherapy. Clin Immunol. 2008; 129: 219-29.
10. Chen G, Emens LA. Chemoimmunotherapy: reengineering tumor immunity. Cancer Immunol Immunother. 2013; 62: 203-16.
11. Zhao Y, Huo M, Xu Z, Wang Y, Huang L. Nanoparticle delivery of CDDO-Me remodels the tumor microenvironment and enhances vaccine therapy for melanoma. Biomaterials. 2015; 68: 54-66.
12. Wang W, Kryczek I, Dostál L, Lin H, Tan L, Zhao L, et al. Effector T cells abrogate stroma-mediated chemoresistance in ovarian cancer. Cell. 2016; 165: 1092-105.
13. Haque A, Banik NL, Ray SK. Emerging role of combination of all-trans retinoic acid and interferon-gamma as chemoimmunotherapy in the management of human glioblastoma. Neurochem Res. 2007; 32: 2203-9.
14. Kullberg M, Martinson H, Mann K, Anchordoquy TJ. Complement C3 mediated targeting of liposomes to granulocytic myeloid derived suppressor cells. Nanomedicine: Nanotechnology, Biology and Medicine. 2015; 11: 1355-63.
15. Gabrilovich DI, Nagaraj S. Myeloid-derived suppressor cells as regulators of the immune system. Nat Rev Immunol. 2009; 9: 162-74.
16. Tacar O, Sriamornsak P, Dass CR. Doxorubicin: an update on anticancer molecular action, toxicity and novel drug delivery systems. J Pharm Pharmacol. 2013; 65: 157-70.
17. Casares N, Pequignot MO, Tesniere A, Ghiringhelli F, Roux S, Chaput N, et al. Caspase-dependent immunogenicity of doxorubicin-induced tumor cell death. J Exp Med. 2005; 202: 1691-701.
18. Zitvogel L, Kepp O, Kroemer G. Immune parameters affecting the efficacy of chemotherapeutic regimens. Nat Rev Clin Oncol. 2011; 8: 151-60.
19. Siddikuzzaman, Guruvayoorappan C, Berlin Grace VM. All trans retinoic acid and cancer. Immunopharmacol Immunotoxicol. 2011; 33: 241-9.
20. Masetti R, Vendemini F, Zama D, Biagi C, Gasperini P, Pession A. All-trans retinoic acid in the treatment of pediatric acute promyelocytic leukemia. Expert Rev Anticancer Ther. 2012; 12: 1191-204.
21. Ginestier C, Wicinski J, Cervera N, Monville F, Finetti P, Bertucci F, et al. Retinoid signaling regulates breast cancer stem cell differentiation. Cell Cycle. 2009; 8: 3297-302.
22. Gudas LJ, Wagner JA. Retinoids regulate stem cell differentiation. J Cell Physiol. 2011; 226: 322-30.
23. Sun R, Liu Y, Li S, Shen S, Du X, Xu C, et al. Co-delivery of all-trans-retinoic acid and doxorubicin for cancer therapy with synergistic inhibition of cancer stem cells. J Control Release. 2015; 213: e94.
24. Kusmartsev S, Cheng F, Yu B, Nefedova Y, Sotomayor E, Lush R, et al. All-trans-retinoic acid eliminates immature myeloid cells from tumor-bearing mice and improves the effect of vaccination. Cancer Res. 2003; 63: 4441-9.
25. Mirza N, Fishman M, Fricke I, Dunn M, Neuger AM, Frost TJ, et al. All-trans-retinoic acid improves differentiation of myeloid cells and immune response in cancer patients. Cancer Res. 2006; 66: 9299-307.
26. Liao W, Lin J, Leonard WJ. Interleukin-2 at the crossroads of effector responses, tolerance, and immunotherapy. Immunity. 2013; 38: 13-25.
27. Rosenberg SA. IL-2: The first effective immunotherapy for human cancer. J Immunol. 2014; 192: 5451-8.
28. Fang Y, Zheng G, Yang J, Tang H, Zhang Y, Kong B, et al. Dual-pore mesoporous carbon@silica composite core–shell nanospheres for multidrug delivery. Angew Chem Int Ed. 2014; 53: 5366-70.
29. Chen Y, Gao Y, Chen H, Zeng D, Li Y, Zheng Y, et al. Engineering inorganic nanoemulsions/nanoliposomes by fluoride-silica chemistry for efficient delivery/co-delivery of hydrophobic agents. Adv Funct Mater. 2012; 22: 1586-97.
30. Niu D, Liu Z, Li Y, Luo X, Zhang J, Gong J, et al. Monodispersed and ordered large-pore mesoporous silica nanospheres with tunable pore structure for magnetic functionalization and gene delivery. Adv Mater. 2014; 26: 4947-53.
31. Pan L, He Q, Liu J, Chen Y, Ma M, Zhang L, et al. Nuclear-targeted drug delivery of TAT peptide-conjugated monodisperse mesoporous silica nanoparticles. J Am Chem Soc. 2012; 134: 5722-5.
32. Fang X, Zhao X, Fang W, Chen C, Zheng N. Self-templating synthesis of hollow mesoporous silica and their applications in catalysis and drug delivery. Nanoscale. 2013; 5: 2205-18.
33. Huang P, Qian X, Chen Y, Yu L, Lin H, Wang L, et al. Metalloporphyrin-encapsulated biodegradable nanosystems for highly efficient magnetic resonance imaging-guided sonodynamic cancer therapy. J Am Chem Soc. 2017; 139: 1275-84.
34. Chen K, Zhang J, Gu H. Dissolution from inside: a unique degradation behaviour of core-shell magnetic mesoporous silica nanoparticles and the effect of polyethyleneimine coating. J Mater Chem. 2012; 22: 22005-12.
35. Zhai W, He C, Wu L, Zhou Y, Chen H, Chang J, et al. Degradation of hollow mesoporous silica nanoparticles in human umbilical vein endothelial cells. J Biomed Mater Res B Appl Biomater. 2012; 100B: 1397-403.
36. Huang P, Chen Y, Lin H, Yu L, Zhang L, Wang L, et al. Molecularly organic/inorganic hybrid hollow mesoporous organosilica nanocapsules with tumor-specific biodegradability and enhanced chemotherapeutic functionality. Biomaterials. 2017; 125: 23-37.
37. Chen Y, Chen H, Guo L, He Q, Chen F, Zhou J, et al. Hollow/rattle-type mesoporous nanostructures by a structural difference-based selective etching strategy. ACS Nano. 2010; 4: 529-39.
38. Park J, Wrzesinski SH, Stern E, Look M, Criscione J, Ragheb R, et al. Combination delivery of TGF-β inhibitor and IL-2 by nanoscale liposomal polymeric gels enhances tumour immunotherapy. Nat Mater. 2012; 11: 895-905.
39. Shen D, Yang J, Li X, Zhou L, Zhang R, Li W, et al. Biphase stratification approach to three-dimensional dendritic biodegradable mesoporous silica nanospheres. Nano Lett. 2014; 14: 923-32.
40. Chen F, Hong H, Shi S, Goel S, Valdovinos HF, Hernandez R, et al. Engineering of hollow mesoporous silica nanoparticles for remarkably enhanced tumor active targeting efficacy. Sci Rep. 2014; 4: 5080.
41. He Q, Shi J, Zhu M, Chen Y, Chen F. The three-stage in vitro degradation behavior of mesoporous silica in simulated body fluid. Microporous Mesoporous Mater. 2010; 131: 314-20.
42. Tan S, Li X, Guo Y, Zhang Z. Lipid-enveloped hybrid nanoparticles for drug delivery. Nanoscale. 2013; 5: 860-72.
43. Ashley CE, Carnes EC, Phillips GK, Padilla D, Durfee PN, Brown PA, et al. The targeted delivery of multicomponent cargos to cancer cells via nanoporous particle-supported lipid bilayers. Nat Mater. 2011; 10: 389-97.
44. Su J, Zhang N, Ho PC. Evaluation of the pharmacokinetics of all-trans-retinoic acid (ATRA) in wistar rats after intravenous administration of ATRA loaded into tributyrin submicron emulsion and its cellular activity on Caco-2 and HepG2 cell lines. J Pharm Sci. 2008; 97: 2844-53.
45. Chung K, Jeong Y, Chung C, Kim D, Kang D. Anti-tumor activity of all-trans retinoic acid-incorporated glycol chitosan nanoparticles against HuCC-T1 human cholangiocarcinoma cells. Int J Pharm. 2012; 422: 454-61.
46. Acquavella N, Kluger H, Rhee J, Farber L, Tara H, Ariyan S, et al. Toxicity and activity of a twice daily high-dose bolus interleukin 2 regimen in patients with metastatic melanoma and metastatic renal cell cancer. J Immunother. 2008; 31: 569-76.
47. Huang H, Shi H, Liu J, Min Y, Wang Y, Wang A, et al. Co-delivery of all-trans-retinoic acid enhances the anti-metastasis effect of albumin-bound paclitaxel nanoparticles. Chem Commun. 2017; 53: 212-5.
48. Wu X, He C, Wu Y, Chen X, Cheng J. Nanogel-incorporated physical and chemical hybrid gels for highly effective chemo-protein combination therapy. Adv Funct Mater. 2015; 25: 6744-55.
49. Marrache S, Tundup S, Harn DA, Dhar S. Ex vivo programming of dendritic cells by mitochondria-targeted nanoparticles to produce interferon-gamma for cancer immunotherapy. ACS Nano. 2013; 7: 7392-402.
50. Shankaran V, Ikeda H, Bruce AT, White JM, Swanson PE, Old LJ, et al. IFN-gamma and lymphocytes prevent primary tumour development and shape tumour immunogenicity. Nature. 2001; 410: 1107-11.

51. Childs RW, Carlsten M. Therapeutic approaches to enhance natural killer cell cytotoxicity against cancer: the force awakens. Nat Rev Drug Discov. 2015; 14: 487-98.
52. Del Vecchio M, Bajetta E, Canova S, Lotze MT, Wesa A, Parmiani G, et al. Interleukin-12: Biological properties and clinical application. Clin Cancer Res. 2007; 13: 4677-85.
53. Calzascia T, Pellegrini M, Hall H, Sabbagh L, Ono N, Elford AR, et al. TNF-alpha is critical for antitumor but not antiviral T cell immunity in mice. J Clin Invest. 2007; 117: 3833-45.
54. Wang X, Li X, Yoshiyuki K, Watanabe Y, Sogo Y, Ohno T, et al. Comprehensive mechanism analysis of mesoporous-silica-nanoparticle-induced cancer immunotherapy. Adv Healthc Mater. 2016; 5: 1169-76.
55. Wang X, Li X, Ito A, Watanabe Y, Sogo Y, Tsuji NM, et al. Stimulation of in vivo antitumor immunity with hollow mesoporous silica nanospheres. Angew Chem Int Ed. 2016; 55: 1899-903.